Nanoscale

ROYAL SOCIETY OF CHEMISTRY

PAPER

View Article Online
View Journal | View Issue

Cite this: *Nanoscale*, 2025, **17**, 17217

Precursor concentration-driven structural evolution and phosphate distribution in electrospun zinc phosphate–carbon nanofibers for lithium-ion storage

Yrysgul Sagynbay,[a,b,c] Long Kong,[d] Zhumabay Bakenov[a,b] and Ayaulym Belgibayeva*[a,c]

Received 24th February 2025,
Accepted 26th June 2025

DOI: 10.1039/d5nr00820d

rsc.li/nanoscale

Reduced zinc phosphate-based carbon composite ($Zn_3P_xO_y$@C) nanofibers are synthesized *via* electrospinning, followed by a two-step heat treatment. The effect of precursor concentration on structural evolution, phosphate distribution, and electrochemical performance is investigated. Solution viscosity influences fiber formation and component interactions, leading to distinct differences in phosphate confinement and porosity. Before annealing, phosphate species are predominant on the surface at low concentrations, balanced at optimal concentrations, and suppressed by polymer accumulation at high concentrations. After annealing, fiber diameters increase at low and optimal concentrations but shrink at high concentrations due to phase redistribution. The optimized nanofibers exhibit a specific surface area of 454 m^2 g^{-1} and 45 wt% carbon, achieving high initial discharge and charge capacities of 1180.6 and 772.6 mAh g^{-1} at 100 mA g^{-1}, respectively, as free-standing lithium-ion battery anodes. These results provide insights into composition-driven nanofiber design for energy storage applications.

Introduction

Zinc phosphate ($Zn_3(PO_4)_2$) is a chemically stable, environmentally benign, and non-toxic material widely used in coatings, biomedical devices, and catalysis due to its structural durability and corrosion resistance.[1–3] Despite these advantages, its potential in lithium-ion batteries (LIBs) has received little attention, due to its inherently low electronic conductivity and moderate theoretical capacity, which restrict its effectiveness as a standalone anode material.[4] As a result, few studies have investigated its electrochemical performance in detail, and its behavior under battery operating conditions remains insufficiently understood.[5,6] Nevertheless, its structural robustness and well-defined phosphate chemistry suggest that zinc phosphate may serve as a stable framework material when combined with conductive phases in composite systems designed to improve lithium storage characteristics.

On the other hand, carbon nanomaterials are widely employed in LIB anodes due to their high electrical conductivity, structural flexibility, and ability to accommodate volume changes during cycling.[7,8] Various engineered carbon frameworks, such as doped graphene, hierarchical porous carbons, and electrospun carbon nanofibers, have demonstrated improvements in charge transport and mechanical stability, making them suitable hosts for embedding less-conductive or electrochemically inactive phases.[9–11] These composite architectures have enabled detailed investigations of structure–property relationships in hybrid anode systems.

In this context, the integration of zinc phosphate into electrospun carbon nanofibers presents a promising route for tuning structural features and improving lithium storage behavior.[12,13] A one-step electrospinning and carbonization approach has previously been employed by our group to prepare a range of phosphate-based nanocomposites.[14,15] In this method, carbon nanofibers serve as conductive and mechanically robust scaffolds that accommodate the incorporation of phosphate species while preserving high surface area and structural uniformity.[16,17] This synthesis strategy also allows systematic control over key material characteristics through variation of precursor composition and processing parameters.[18]

Numerous factors intricately influence the formation of nanofibers during electrospinning, encompassing a spectrum

[a]*National Laboratory Astana, Kabanbay Batyr Ave. 53, Astana 010000, Kazakhstan. E-mail: ayaulym.belgibayeva@nu.edu.kz*
[b]*Department of Chemical and Materials Engineering, School of Engineering and Digital Sciences, Nazarbayev University, Kabanbay Batyr Ave. 53, Astana 010000, Kazakhstan*
[c]*Institute of Batteries, Kabanbay Batyr Ave. 53, Astana 010000, Kazakhstan*
[d]*Institute of Flexible Electronics (IFE), Northwestern Polytechnical University, Xi'an, Shaanxi 710129, China*

of considerations from polymer characteristics, solution properties, processing parameters, to environmental conditions.[19,20] These factors include the molecular weight and polymer–solvent compatibility, solution concentration, viscosity, and conductivity, as well as processing parameters like voltage and flow rates, alongside environmental variables such as temperature and relative humidity.[17] Of particular significance, the polymer concentration exerts a direct influence on the formation of smooth and robust fibers,[21] underscoring its pivotal role in dictating the quality of the electrospun products. Moreover, the electrospinning solution concentration impacts critical parameters including pore volume, specific surface area, and rate capability,[22] thereby shaping the performance characteristics of the resulting materials. Therefore, understanding how precursor concentration governs the structural evolution of zinc phosphate during electrospinning and heat treatment is essential for guiding the design of effective composite anodes.

In this work, the effect of precursor concentration on the structural evolution, phosphate distribution, and electrochemical performance of reduced zinc phosphate–carbon composite ($Zn_3P_xO_y$@C) nanofibers is investigated. The composites were synthesized *via* a single-step electrospinning and subsequent heat treatment process, enabling controlled incorporation of the active phase into a conductive carbon framework. By systematically varying the precursor concentration, its influence on the morphology, chemical structure, and lithium storage behavior is examined using a combination of structural and electrochemical characterization techniques.

Experimental

Synthesis of $Zn_3P_xO_y$@C nanofibers

To study the effect of the solution concentration on the synthesis of reduced zinc phosphate-based carbon composite nanofibers, four solutions of different concentrations were prepared, as listed in Table 1, keeping the polymer : precursor and Zn : P ratios constant at 1 : 1. An appropriate amount of polyvinylpyrrolidone (PVP, M_w = 1 300 000, Sigma-Aldrich) was dissolved in 6 ml of absolute ethanol (Labochem International) and stirred with a magnetic stirrer at 600 rpm. Simultaneously, a corresponding amount of zinc nitrate hexahydrate ($Zn(NO_3)_2{\cdot}6H_2O$, 98%, Thermo Scientific) was dissolved in 2 ml of distilled water, followed by the addition of phosphoric acid (H_3PO_4, 85%, Sigma-Aldrich). This solution was hand-shaken, introduced to the PVP solution using a pipette, and stirred magnetically for ~18 hours at room temperature.

The resulting solutions of different concentrations were loaded into a 20 ml syringe, and electrospun at a flow rate of 1 ml h^{-1} and a voltage of 18 kV, with a tip-to-collector distance of 10 cm. The fibers were collected on aluminium foil using a drum collector, rotating at 100 rpm. After electrospinning, the samples were dried at 120 °C for 12 hours in air and denoted as $Zn_3(PO_4)_2$@PVP.

The $Zn_3(PO_4)_2$@PVP samples were further pre-oxidized at 280 °C for 1 hour in a muffle furnace, annealed in a horizontal tube furnace for 1 hour at 750 °C under a flowing N_2 + H_2 (4%) atmosphere with a heating rate of 5 °C min^{-1}, and denoted as $Zn_3P_xO_y$@C, as indicated in Table 1.

Physical characterization

The viscosity of the electrospinning solutions was measured with a rheometer (Anton Paar, MCR 102e). Conductivity was determined using a conductometer (Mettler Toledo, SevenCompact S230-Std-Kit). Chemical bonds were identified by FTIR (Nicolet iS10 FT-IR spectrometer). Thermal characteristics were examined by thermogravimetry–differential thermal analysis (TG-DTA, Rigaku Corp. Thermo Plus TG8120) in air.

Structure and morphology of nanofibers were observed using a scanning electron microscope (SEM, ZEISS Crossbeam 540) and an energy dispersive spectrometer (EDS, JEOL, JSM-IT200(LA)) The diameter distribution of nanofibers was calculated by measuring 500 fibers per sample using the open-source image processing software ImageJ. Crystal structure of the annealed samples was examined by X-ray diffraction (XRD, MiniFlex600 Benchtop, Rigaku Corporation) with an X-ray generator of 600 W (40 kW – 15 mA), in the range of 15–60° with 0.01° step and 10° min^{-1} speed using Cu Kα radiation (λ = 1.5406 Å). The degree of graphitization was determined by Raman spectroscopy (LabRAM HR Evolution & OmegaScope). The surface composition was examined using an X-ray photoelectron spectrometer (XPS, NEXSA, Thermo Scientific). The carbon content was calculated by CHNS (Elementar Analysensysteme GmbH, 15061000) analysis. Pore size distribution was determined using the Barrett–Joyner–Halenda (BJH) method based on N_2 adsorption–desorption isotherms (recorded at the temperature of liquid N_2), while the specific surface area was calculated using the Brunauer–Emmett–Teller (BET) method (TRISTAR II PLUS).

Table 1 Masses of precursors used at different concentration coefficients (C) and corresponding sample names

	Mass of precursors (g)			Sample name	
Concentration coefficient	PVP	$Zn(NO_3)_2{\cdot}6H_2O$	H_3PO_4	After electrospinning	After annealing
1.0C	0.430	0.330	0.129	$Zn_3(PO_4)_2$@PVP-1.0	$Zn_3P_xO_y$@C-1.0
1.1C	0.473	0.363	0.142	$Zn_3(PO_4)_2$@PVP-1.1	$Zn_3P_xO_y$@C-1.1
1.2C	0.516	0.396	0.155	$Zn_3(PO_4)_2$@PVP-1.2	$Zn_3P_xO_y$@C-1.2
1.3C	0.559	0.429	0.168	$Zn_3(PO_4)_2$@PVP-1.3	$Zn_3P_xO_y$@C-1.3

Electrochemical characterization

The electrochemical properties of $Zn_3P_xO_y$@C samples were measured using CR2032 coin-type cells assembled in a glovebox filled with high-purity Ar (H_2O and O_2 contents of <0.1 ppm). Li chips were used as the reference electrode and free-standing $Zn_3P_xO_y$@C samples with a mass loading of 1.1 ± 0.2 mg cm^{-2} were directly used as the anode without any coating procedure. 1 M $LiPF_6$ dissolved in a mixture of ethylene carbonate, diethyl carbonate, and ethyl methyl carbonate (EC : DEC : EMC = 1 : 1 : 1, vol.) was used as the electrolyte.

Cyclic voltammetry (CV) was performed over the potential range of 0.01–3.0 V *vs.* Li/Li^+ at a scan rate of 0.1 mV s^{-1} on a potentiostat/galvanostat (BioLogic VMP3). Charge–discharge profiles and cyclability at 100 mA g^{-1}, and rate-capability between 100 and 4000 mA g^{-1} were recorded on a NEWARE battery testing system (BTS4000) in the same potential range.

The current densities were calculated based on the total mass of the electrodes, while capacities were calculated based on the mass of pure $Zn_3P_xO_y$.

Results and discussion

Effect of solution concentration on the structure of precursor fibers

The concentration of the electrospinning solution influences its rheological properties, including viscosity and electrical conductivity, which in turn affect the fiber formation.[19] As shown in Fig. 1a, the linear shear stress–shear rate relationship indicates Newtonian fluid behavior. Viscosity increased with concentration (Fig. 1b), with the 1.2C solution showing the most stable values, as indicated by narrower error bars. This can be attributed to the optimal concentration regime, where solute–solute and solute–solvent interactions are balanced. At this concentration, polymer chains are sufficiently entangled, and ionic species are uniformly dispersed, minimizing local heterogeneities and ensuring consistent flow behavior. In contrast, lower concentrations (*e.g.*, 1.0C) lack molecular connectivity, while higher concentrations (*e.g.*, 1.3C) may experience partial aggregation or phase separation, both leading to viscosity instability.

Electrical conductivity also increased proportionally with concentration (Fig. 1c). These changes are critical to electrospinning, as higher viscosity generally leads to thicker fibers, while increased conductivity promotes jet stretching and finer fiber formation.[23,24] Thus, optimizing the precursor concentration is essential for controlling fiber morphology and ensuring stable electrospinning.

The effect of the solution concentration on the morphology of electrospun samples was further studied by SEM. Fig. 2a shows that all four concentrations produce uniform fibrous structures, while Fig. 2b shows clear variations in fiber diameter with concentration. The highest concentration, $Zn_3(PO_4)_2$@PVP-1.3, produced the thickest fibers (236 nm), consistent with the viscosity trend observed in Fig. 1b. $Zn_3(PO_4)_2$@PVP-1.1 yielded the finest fibers (88 nm), whereas $Zn_3(PO_4)_2$@PVP-1.0 exhibited a slightly larger average diameter (115 nm), deviating from the expected trend. This anomaly may stem from fluctuations in solution behavior, particularly the pronounced viscosity instability observed for 1.0C, which at times surpasses that of 1.1C. Overall, the results confirm that higher solution viscosity generally leads to increased fiber diameter after electrospinning.[19]

The surface elemental distribution of $Zn_3(PO_4)_2$@PVP samples is presented in Fig. 2c and summarized in Table 2. Variations in the content of carbon (C), nitrogen (N), and phosphorus (P) are observed across the samples. With increasing solution concentration, C and N contents increase while the P content decreases, suggesting surface enrichment of PVP and a corresponding reduction in surface phosphate concentration. This may result from changes in phase separation behavior during electrospinning and drying. $Zn_3(PO_4)_2$@PVP-1.0 deviates from this trend, exhibiting an unexpected elemental composition. This anomaly may arise from non-uniform component distribution, differences in morphology, or altered interactions between PVP and phosphate at lower concentrations. These results highlight the complex relationship between solution concentration, electrospinning dynamics, and surface composition, reinforcing the influence of rheological properties on fiber morphology.

The influence of concentration on the chemical composition and interactions within as-spun $Zn_3(PO_4)_2$@PVP samples was analyzed using FTIR, as shown in Fig. 3a. Prominent peaks at 1610 cm^{-1} and 1293 cm^{-1} correspond to the C=O and C–N stretching vibrations of the pyrrolidone ring in PVP. The position of the C=O band shifts with concen-

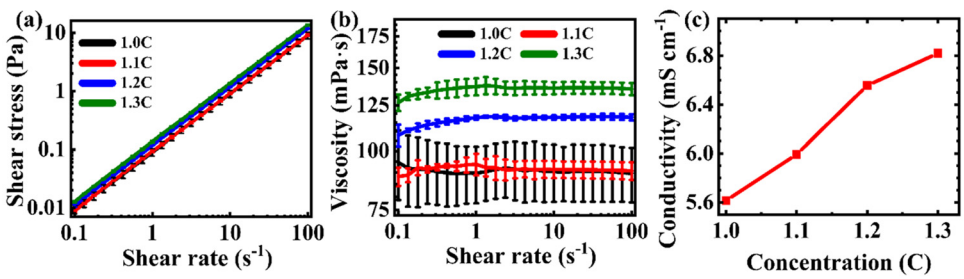

Fig. 1 (a) Flow curve of shear stress *vs* shear rate, (b) viscosity as a function of the shear rate and (c) conductivity *vs* concentration graphs of electrospinning solutions of different concentrations.

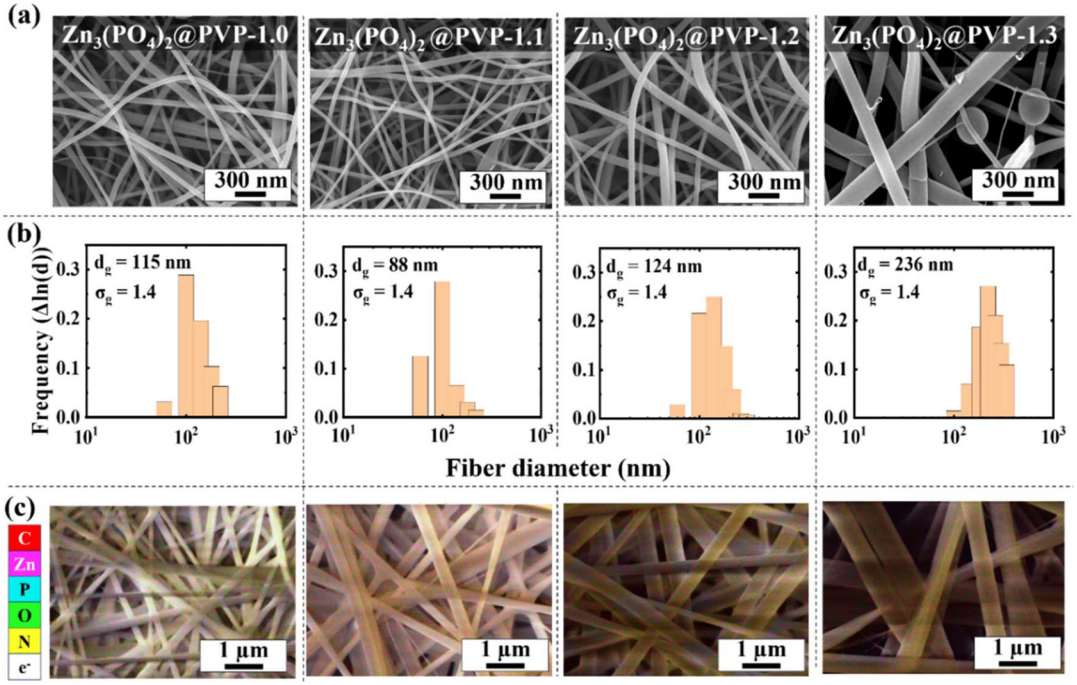

Fig. 2 (a) SEM images, (b) diameter distribution, and (c) EDS mapping of as-spun and dried $Zn_3(PO_4)_2$@PVP precursor fibers prepared from solutions of different concentrations.

Table 2 Surface composition of as-spun and dried precursor fibers prepared from solutions of different concentrations determined by EDS mapping

Sample name	C (wt%)	Zn (wt%)	P (wt%)	O (wt%)	N (wt%)
$Zn_3(PO_4)_2$@PVP-1.0	48.9	14.2	8.1	16.5	12.3
$Zn_3(PO_4)_2$@PVP-1.1	48.3	14.5	9.6	16.5	11.0
$Zn_3(PO_4)_2$@PVP-1.2	49.0	14.5	7.5	15.6	13.4
$Zn_3(PO_4)_2$@PVP-1.3	58.1	9.6	5.2	12.1	15.1

tration, reflecting changes in the molecular environment. A leftward shift at lower concentrations suggests stronger bonding due to reduced interactions, while a rightward shift at higher concentrations indicates weaker bonding, likely caused by stronger interactions with surrounding species.

Additional variations appear in the regions of 1426–1471 cm^{-1} (C–C stretching) and 1079–1292 cm^{-1} (P–O or PO_4^{3-} stretching).[24,25] $Zn_3(PO_4)_2$@PVP-1.2 exhibits the lowest peak intensities, which may reflect stronger coordination or cross-linking between PVP and phosphate species. In contrast, $Zn_3(PO_4)_2$@PVP-1.1 and 1.3 show more intense C–N peaks, indicating a greater presence of free functional groups. These findings confirm that the precursor concentration influences molecular interactions within the fibers, affecting their chemical environment during electrospinning.

After electrospinning and drying, the $Zn_3(PO_4)_2$@PVP samples were pre-oxidized in air at 280 °C. To examine how precursor concentration affects thermal decomposition during this step, TG-DTA was performed on the dried fibers (Fig. 3b). The initial weight loss below 200 °C is attributed to the evapor-

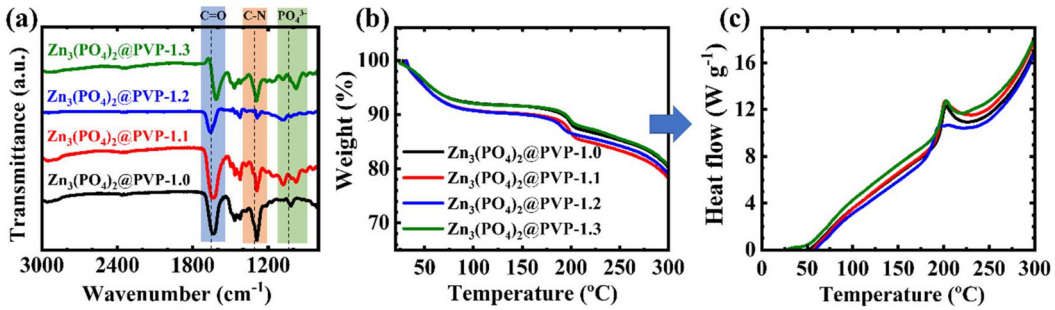

Fig. 3 (a) FTIR, (b) TGA and (c) DTA of as-spun and dried precursor fibers prepared from solutions of different concentrations.

ation of adsorbed and bound water, while a more significant loss near 200 °C corresponds to the decomposition of crystal hydrates, as $Zn_3(PO_4)_2$ can coordinate up to four moles of H_2O.[26,27] $Zn_3(PO_4)_2$@PVP-1.1 and $Zn_3(PO_4)_2$@PVP-1.2 exhibit greater weight loss in this region, indicating higher water content compared to $Zn_3(PO_4)_2$@PVP-1.0 and $Zn_3(PO_4)_2$@PVP-1.3. Between 200 and 300 °C, the decomposition and stabilization of PVP occur, with $Zn_3(PO_4)_2$@PVP-1.0 showing greater weight loss compared to $Zn_3(PO_4)_2$@PVP-1.3, suggesting concentration-dependent differences in the decomposition pathways.

Fig. 3c shows the corresponding DTA curves, where exothermic peaks indicate energy release associated with thermal events observed in TGA. The exothermic peaks around 200 °C reflect energy release from crystal hydrate decomposition. Notably, $Zn_3(PO_4)_2$@PVP-1.2 exhibits the weakest exothermic response, potentially indicating reduced energy release due to interactions among hydrates, PVP, and phosphate species. These results demonstrate that the precursor concentration influences the thermal behavior of the fibers during pre-oxidation, affecting both water content and PVP decomposition characteristics.

Effect of solution concentration on the structure of final products

The pre-oxidized $Zn_3(PO_4)_2$@PVP samples were further annealed at 750 °C under an N_2 + H_2 atmosphere to induce reduction and carbonization. Fig. 4a presents the XRD patterns of the resulting $Zn_3P_xO_y$@C composites prepared from solutions of varying concentrations. The primary crystalline phase is identified as monoclinic α-$Zn_3(PO_4)_2$ (space group $A2/a$), with partial reduction to monoclinic $Zn_2P_2O_7$ of the same space group. This coexistence indicates that the reducing environment promotes phosphate transformation while retaining the structural framework.

Concentration-dependent differences in phase composition are observed. In $Zn_3P_xO_y$@C-1.3 and $Zn_3P_xO_y$@C-1.1, additional peaks at 29.68° and 25.37°, respectively, correspond to monoclinic β-$Zn_3(PO_4)_2$ (space group $P2_1/a$), suggesting that precursor concentration influences phase stability and crystallization pathways. Higher concentrations may lead to localized thermal or chemical gradients that favor β-phase formation. Differences in diffraction peak intensity and sharpness across samples further indicate variation in crystallinity. Samples

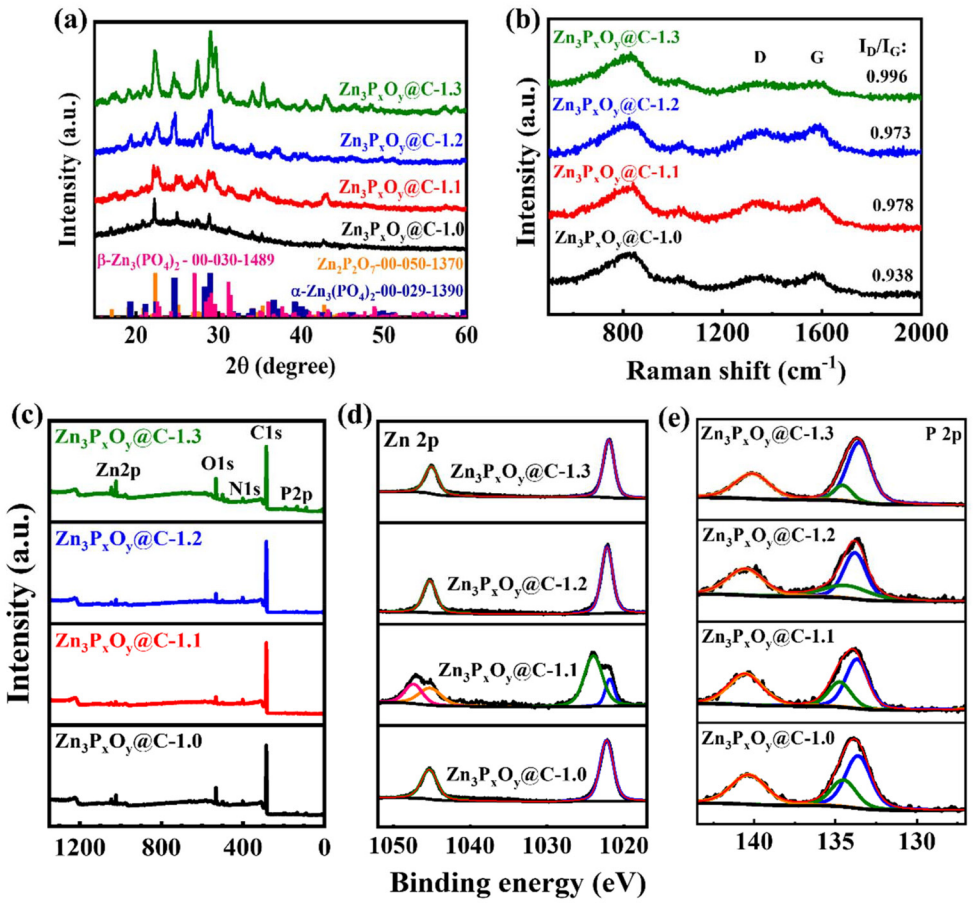

Fig. 4 (a) XRD patterns; (b) Raman spectra; (c) XPS survey spectra and high resolution (d) Zn 2p and (e) P 2p XPS spectra of $Zn_3P_xO_y$@C samples prepared at different solution concentrations.

from higher-concentration solutions exhibit more intense and sharper peaks, consistent with enhanced crystallization due to increased Zn and P contents. In contrast, broader peaks in low-concentration samples suggest smaller crystallites or partial amorphization resulting from limited precursor availability during annealing.

Fig. 4b shows the Raman spectra of the $Zn_3P_xO_y$@C samples, highlighting the characteristic D and G bands at 1360 cm^{-1} and 1590 cm^{-1}, respectively. The intensity ratio of I_D/I_G serves as an indicator of the degree of graphitization, with lower ratios reflecting higher graphitization and structural order. Among the samples, $Zn_3P_xO_y$@C-1.2 shows the second lowest I_D/I_G ratio (0.973) after $Zn_3P_xO_y$@C-1.0, suggesting a higher degree of graphitization. In contrast, $Zn_3P_xO_y$@C-1.3 exhibits the highest I_D/I_G ratio (0.996), indicating greater structural disorder.

The correlation between XRD and Raman results suggests that the precursor concentration affects both crystalline phase formation and the carbon structure. Higher concentrations promote phosphate crystallization but result in more disordered carbon, while moderate concentrations, such as in $Zn_3P_xO_y$@C-1.2, achieve a balance between carbon ordering and inorganic phase formation. These structural differences are expected to influence the electrochemical performance by affecting conductivity, ion transport, and material stability.

To further investigate the composition and chemical states in $Zn_3P_xO_y$@C samples, XPS analysis was performed. The survey spectra, presented in Fig. 4c, show clear signals for Zn $2p_{1/2}$, Zn $2p_{3/2}$, O 1s, N 1s, C 1s and P 2p, confirming the presence of these elements at the surface. The detection of nitrogen suggests the retention of nitrogen-containing species from the PVP precursor after carbonization, while the strong P and O signals confirm the persistence of phosphate species after thermal treatment.

Fig. 4d focuses on the Zn 2p region, exhibiting two characteristic peaks at 1045.08 eV and 1021.98 eV, corresponding to Zn $2p_{1/2}$ and Zn $2p_{3/2}$, respectively, with a spin–orbit splitting of ~23 eV, consistent with Zn^{2+}.[1] This confirms the preservation of divalent zinc in $Zn_3P_xO_y$@C-1.2 and 1.3. In contrast, partial zinc reduction is observed in $Zn_3P_xO_y$@C-1.1.

The partial reduction of Zn^{2+} observed exclusively in $Zn_3P_xO_y$@C-1.1 may be attributed to the fine fiber morphology and less uniform phosphate distribution originating from the low-viscosity precursor solution. These features likely increased surface area and gas accessibility during annealing, facilitating stronger local reducing conditions on the fiber surface. In contrast, the denser and more uniform structures of the other samples suppressed excessive Zn reduction on the surface.

The high-resolution P 2p spectra, shown in Fig. 4e, exhibit a well-resolved doublet at 134.45 eV and 133.7 eV, assigned to $P_2O_7^{4-}$ (pyrophosphate) and PO_4^{3-} (phosphate), respectively, with varying intensity ratios across samples.[5] This observation aligns with the XRD results, confirming the coexistence of α-$Zn_3(PO_4)_2$, β-$Zn_3(PO_4)_2$, and $Zn_2P_2O_7$ phases.

Overall, the XPS analysis supports the phase composition identified by XRD and reveals that nitrogen-doped carbon, divalent zinc, and stable phosphate species are retained after reduction and carbonization. These chemical features are expected to influence the electrochemical performance of the $Zn_3P_xO_y$@C materials.

The elemental composition of $Zn_3P_xO_y$@C samples, determined by CHNS analysis and shown in Table 3, reveals clear trends in carbon, hydrogen, and nitrogen contents across different precursor concentrations. Among them, $Zn_3P_xO_y$@C-1.2 exhibits the highest carbon content at 45 wt%, suggesting a more efficient carbon retention during carbonization. In contrast, $Zn_3P_xO_y$@C-1.3 shows the lowest carbon content (39 wt%), indicating possible differences in carbonization efficiency or stronger interactions between the carbon matrix and inorganic phases at higher concentrations. The nitrogen content also varies, increasing from 1 wt% in $Zn_3P_xO_y$@C-1.0 to a maximum of 3 wt% in $Zn_3P_xO_y$@C-1.2, before slightly decreasing in $Zn_3P_xO_y$@C-1.3. This trend suggests the enhanced retention of nitrogen-containing species from PVP at intermediate concentrations, which may influence both structural and electrochemical properties. These findings highlight the role of precursor concentration in determining the carbon and nitrogen content of the final composites. The higher carbon content in $Zn_3P_xO_y$@C-1.2 may contribute to improved electronic conductivity and structural stability, which are critical factors in energy storage applications.

Fig. 5a and b present SEM images and corresponding diameter distributions of $Zn_3P_xO_y$@C samples after annealing. Among all samples, $Zn_3P_xO_y$@C-1.2 exhibits the most uniform fiber morphology with consistent diameters and smooth surfaces, indicating a stable structural transformation during annealing. The fibers maintain their integrity without noticeable deformation, and the diameter distribution is relatively narrow, suggesting uniform thermal behavior and controlled phase evolution. This uniformity may result from balanced precursor composition and cross-linking interactions (as supported by Fig. 3a), which facilitate even carbonization and integration of inorganic phases. In contrast, $Zn_3P_xO_y$@C-1.1 and $Zn_3P_xO_y$@C-1.3 show distinct morphological features, including spherical agglomerates, likely formed through localized crystallization or phase segregation. While most samples exhibit increased diameters after annealing—attributed to gas evolution and pore formation—$Zn_3P_xO_y$@C-1.3 exhibits a decrease, suggesting densification, structural collapse, or limited thermal stability of the polymer–inorganic network, potentially due to excess surface PVP (see Fig. 2c and Table 2).

The elemental mapping shown in Fig. 5c provides further insights into the distribution of elements within the annealed

Table 3 Elemental composition determined by CHNS analysis

Sample	C (wt%)	H (wt%)	N (wt%)
$Zn_3P_xO_y$@C-1.0	40	1	1
$Zn_3P_xO_y$@C-1.1	41	1	2
$Zn_3P_xO_y$@C-1.2	45	1	3
$Zn_3P_xO_y$@C-1.3	39	1	2

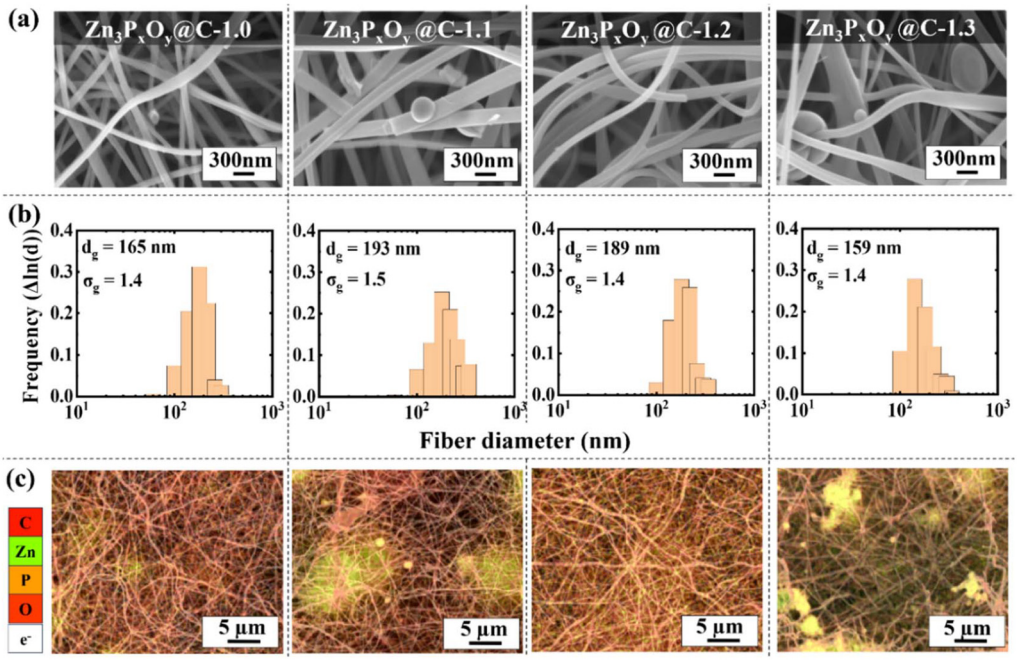

Fig. 5 (a) SEM images, (b) diameter distribution, and (c) EDS mapping of $Zn_3P_xO_y$@C samples.

nanofibers. $Zn_3P_xO_y$@C-1.2 demonstrates a uniform distribution of Zn, P, O, and C, indicating successful incorporation of inorganic species into the carbon matrix. In contrast, $Zn_3P_xO_y$@C-1.1 and $Zn_3P_xO_y$@C-1.3 exhibit surface-localized agglomerates, reflecting inhomogeneous elemental dispersion likely caused by phase separation and preferential nucleation during annealing.

These observations highlight the critical role of precursors in controlling fiber morphology, diameter, and elemental homogeneity. The well-defined and uniformly distributed structure of $Zn_3P_xO_y$@C-1.2 positions it as a promising candidate for applications demanding high structural integrity and functional performance.

Fig. 6a shows the nitrogen adsorption/desorption isotherms of $Zn_3P_xO_y$@C samples synthesized from different precursor concentrations. All samples exhibit a steep uptake at low relative pressures (P/P_0), followed by a plateau, which is characteristic of type II isotherms—typical for microporous materials.[28] The sharp rise in adsorption at low pressures indicates the presence of micropores, while the gradual leveling off at higher pressures suggests the filling of larger pore structures.[22,28]

Among the samples, $Zn_3P_xO_y$@C-1.2 exhibits the highest nitrogen uptake, indicating superior porosity and a larger specific surface area. This enhanced adsorption suggests the formation of a well-developed porous network, which is advantageous for gas adsorption and may facilitate improved ion transport in electrochemical systems.

Fig. 6b presents the corresponding pore size distributions. $Zn_3P_xO_y$@C-1.2 demonstrates the highest pore volume and

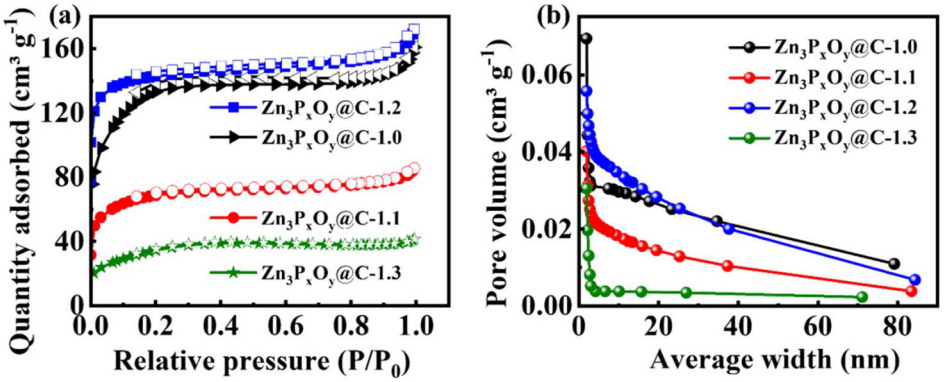

Fig. 6 (a) N_2 adsorption and desorption isotherms and (b) pore size distribution in $Zn_3P_xO_y$@C samples.

average pore width, alongside a remarkably high specific surface area of 454 m^2 g^{-1}. All samples show significant porosity within the 2–50 nm range, confirming the dominance of mesoporous structures—beneficial for electrolyte penetration and fast ion diffusion.

The superior textural properties observed in $Zn_3P_xO_y$@C-1.2 are attributed to its optimized precursor concentration, which likely promotes uniform phase distribution and controlled gas evolution during thermal treatment. These features are expected to significantly enhance the electrochemical performance by improving ionic accessibility and minimizing diffusion limitations.

The impact of precursor concentration on fiber formation, structural evolution, and phosphate distribution within $Zn_3P_xO_y$@C nanofibers can be comprehensively understood by considering the sequence of changes from solution properties to the final annealed fibers as illustrated in Fig. 7. Among all samples, $Zn_3P_xO_y$@C-1.2, prepared from an optimally balanced solution, shows uniform phosphate distribution both inside and outside the fibers after electrospinning. This uniformity is likely due to effective cross-linking between phosphate groups and PVP, enhancing structural cohesion and stability during subsequent thermal treatments.

During pyrolysis, $Zn_3P_xO_y$@C-1.2 retains structural integrity despite fiber expansion caused by gas evolution and pore formation. The uniform phosphate distribution is preserved, supported by SEM-EDS mapping and high surface area measurements, indicating effective integration of phosphate within the carbon matrix.

In contrast, $Zn_3P_xO_y$@C-1.1 and $Zn_3P_xO_y$@C-1.3 show less uniform phosphate distribution, with agglomeration primarily on fiber surfaces. This can be attributed to weaker phosphate-PVP interactions in $Zn_3P_xO_y$@C-1.1 and phase segregation at higher precursor concentrations in $Zn_3P_xO_y$@C-1.3. Additionally, fiber shrinkage in $Zn_3P_xO_y$@C-1.3 suggests densification due to phosphate aggregation.

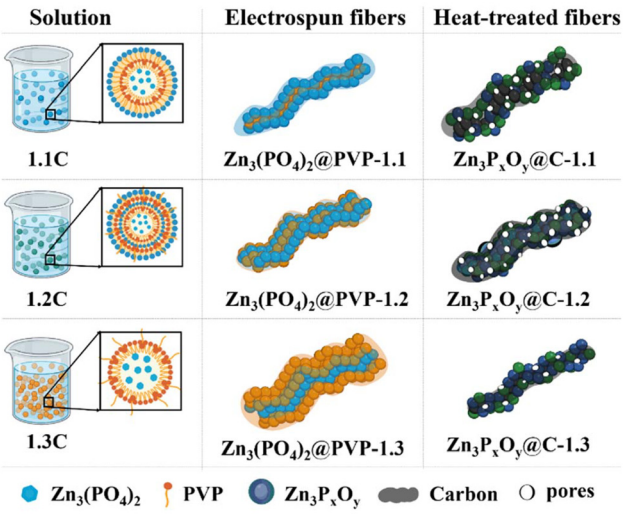

Fig. 7 Illustration of the possible effect mechanism of the precursor concentration on the formation of $Zn_3P_xO_y$@C fibers. Created in BioRender. Belgibayeva, A. (2025) https://BioRender.com/6ex1y0v.

Effect of solution concentration on the electrochemical properties

Fig. 8a shows the initial CV curves of $Zn_3P_xO_y$@C samples prepared from four different precursor concentrations. Variations in the shape and intensity of the redox peaks reflect differences in composition, structure, and electrochemical behavior among the samples. $Zn_3P_xO_y$@C-1.2 exhibits pronounced redox peaks, indicating enhanced electrochemical activity and improved utilization of the active material. During the first cathodic scan of $Zn_3P_xO_y$@C-1.2, distinct peaks appear at 1.4 V and 0.55 V, corresponding to electrolyte decomposition and solid electrolyte interphase (SEI) formation, followed by further interfacial reactions associated with electrode activation. A smaller cathodic peak near 0.4 V, likely reflects conversion-type reactions involving reduced Zn–P–O species during lithium insertion. At potentials below 0.1 V, a broad cathodic feature is observed, which may be attributed to deep lithiation and strong lithium interaction with reduced Zn-containing phases. During the subsequent anodic sweep, oxidation peaks suggest the partial reversibility of these reduction processes, including reconversion reactions and SEI modification. The well-defined redox features in $Zn_3P_xO_y$@C-1.2 indicate favorable kinetics and improved interfacial stability. These observations underscore the influence of precursor concentration on the structural evolution and electrochemical performance of the resulting nanofibers.

Fig. 8b presents the galvanostatic charge–discharge profiles of $Zn_3P_xO_y$@C samples, highlighting their initial specific capacities. The shapes and positions of the plateaus observed during the charge–discharge cycles align well with the redox peaks identified in the CV curves, confirming the consistency of the electrochemical processes across both techniques. Among the samples, $Zn_3P_xO_y$@C-1.2 demonstrates the highest initial specific capacity, which is consistent with its pronounced oxidation–reduction peaks observed in the CV analysis. Specifically, $Zn_3P_xO_y$@C-1.2 achieves an initial discharge capacity of 1180.6 mAh g^{-1} and a charge capacity of 772.6 mAh g^{-1}, resulting in an initial coulombic efficiency of 65.43%. The high discharge capacity reflects the effective lithium-ion storage within the active material.

Fig. 8c shows the cycling performance of $Zn_3P_xO_y$@C samples over 100 cycles. $Zn_3P_xO_y$@C-1.2 initially exhibits a noticeable capacity degradation during the first 40 cycles, which can be attributed to factors such as SEI layer formation, irreversible side reactions, and structural rearrangements within the electrode. Following this decline, the capacity gradually increases, reaching 434 mAh g^{-1} after 100 cycles. This recovery suggests partial reactivation of the electrode material or improved lithium-ion transport pathways as structural stabilization occurs during cycling. However, the final capacity of $Zn_3P_xO_y$@C-1.2 is not significantly higher compared to the other samples. After 100 cycles, all samples show comparable capacities, indicating that the initial advantage of

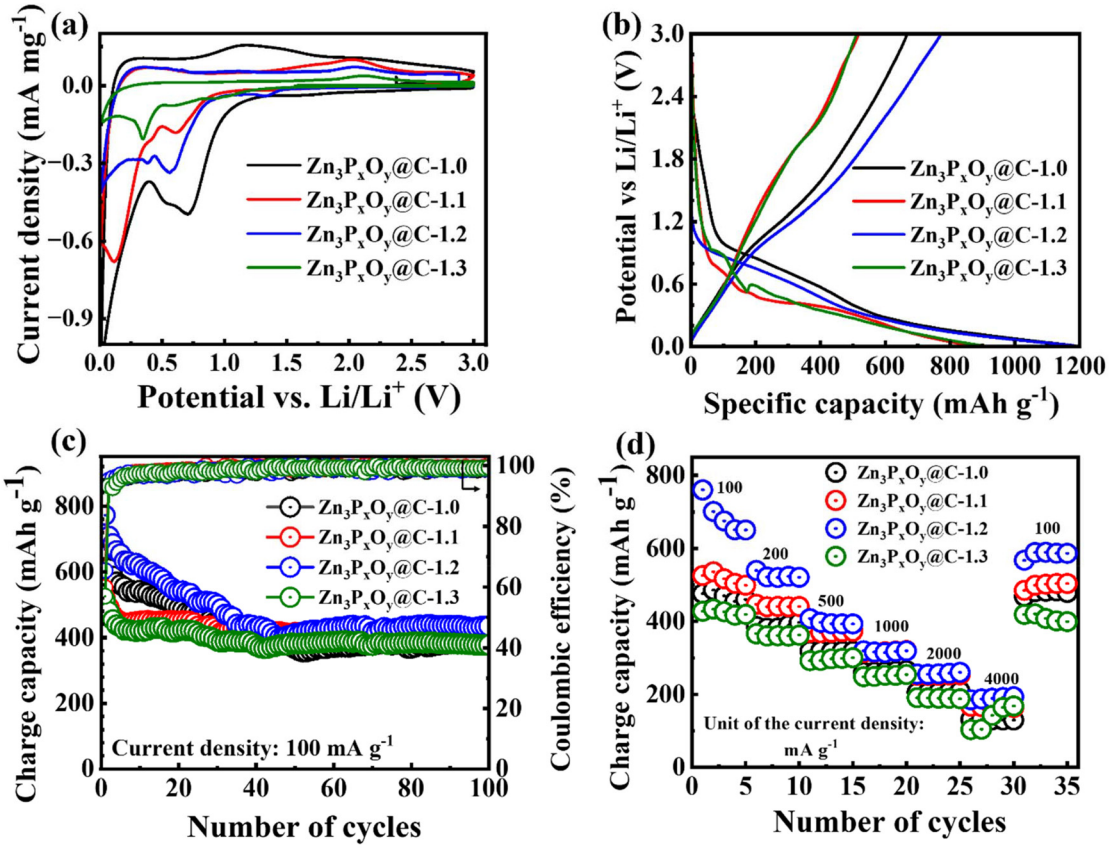

Fig. 8 (a) CV curves, (b) charge–discharge profiles, (c) cycle performance and (d) rate capability of $Zn_3P_xO_y$@C samples.

$Zn_3P_xO_y$@C-1.2 in terms of specific capacity diminishes over prolonged cycling. This convergence suggests that long-term cycling stability is influenced by additional factors, such as electrode degradation, SEI instability, and the progressive loss of active material.

Fig. 8d illustrates the rate capability of $Zn_3P_xO_y$@C samples at current densities ranging from 100 to 4000 mA g^{-1}. All samples exhibited a gradual decline in specific capacity with increasing current density, reflecting the expected limitations in lithium-ion diffusion and charge transfer kinetics under high-rate conditions. $Zn_3P_xO_y$@C-1.2 maintained higher capacities than other samples throughout the intermediate current range, indicating improved electrode kinetics and structural features that facilitated more efficient ion transport. However, at the highest current density of 4000 mA g^{-1}, the differences between the samples became negligible, suggesting that intrinsic transport barriers and electrode polarization effects dominated the performance at this rate. Upon returning to 100 mA g^{-1}, $Zn_3P_xO_y$@C-1.2 retained a capacity of 588 mAh g^{-1}, indicating good reversibility and structural stability after high-rate cycling. In contrast, the other samples showed significantly lower reversible capacities, highlighting the superior structural resilience of $Zn_3P_xO_y$@C-1.2.

Notably, $Zn_3P_xO_y$@C-1.0 and $Zn_3P_xO_y$@C-1.3 exhibit inconsistent electrochemical behavior. For $Zn_3P_xO_y$@C-1.0, the variation in initial capacities at same current densities—ranging from above 600 mAh g^{-1} in Fig. 8c to slightly over 400 mAh g^{-1} in Fig. 8d—can be attributed to instability in the rheological properties of the precursor solution, which led to irregularities in fiber morphology and phosphate distribution, as previously discussed. In the case of $Zn_3P_xO_y$@C-1.3, the lower and fluctuating capacities are likely a result of non-uniform phosphate distribution within the fibers, which was confirmed by surface composition analysis. These structural inconsistencies may have led to uneven electrochemical activity and hindered lithium-ion transport, thereby reducing the reproducibility and reliability of performance across different test conditions.

These results underscore the influence of precursor concentration on the initial electrochemical behavior of $Zn_3P_xO_y$@C composites and motivate further investigation into their long-term cycling mechanisms.

Conclusions

Reduced zinc phosphate-based carbon composite ($Zn_3P_xO_y$@C) nanofibers were successfully synthesized *via* a concentration-controlled one-pot electrospinning and carbothermal reduction approach, employing zinc nitrate, phosphoric acid, and polyvinylpyrrolidone (PVP) as precursors. The

concentration of the electrospinning solution played a critical role in determining the fiber morphology, phosphate distribution, and structural characteristics of the resulting composites. Nanofibers derived from an optimally balanced solution exhibited uniform phosphate dispersion, controlled fiber expansion, and enhanced porosity—features likely promoted by favorable interactions between phosphate species and PVP. These characteristics translated into improved material stability and enhanced initial electrochemical performance, with $Zn_3P_xO_y$@C-1.2 achieving discharge and charge capacities of 1180.6 mAh g^{-1} and 772.6 mAh g^{-1}, respectively. However, structural and compositional deviations at non-optimal concentrations led to either surface agglomeration of phosphates or abnormal fiber shrinkage during annealing, limiting electrochemical performance. Despite the initial advantages, capacity degradation was observed within the first 40 cycles, and all samples converged to comparable capacities (~434 mAh g^{-1}) after 100 cycles. These results demonstrate the importance of precise precursor concentration control in tuning the architecture and functionality of phosphate–carbon nanofiber composites, while also highlighting the need for further structural and interfacial optimization to improve long-term cycling stability and rate performance for lithium-ion storage applications.

Author contributions

Yrysgul Sagynbay: investigation, data curation, visualization, and writing – original draft; Long Kong: investigation and writing – review & editing; Zhumabay Bakenov: resources, supervision, validation, and writing – review & editing; and Ayaulym Belgibayeva: conceptualization, methodology, visualization, project administration, resources, supervision, funding acquisition, and writing – review & editing.

Conflicts of interest

There are no conflicts to declare.

Data availability

The data supporting this article have been included in the figures and tables within the text.

Acknowledgements

This work was supported by the Science Committee of the Ministry of Science and Higher Education of the Republic of Kazakhstan [grant numbers AP19675260, BR21882402, and BR24992766]. The authors are grateful to the staff of the Core Facilities of the Nazarbayev University for their assistance in conducting the physical characterization studies of samples, Dr Sagyn Omirbekov (National Laboratory Astana) for viscosity measurements, Rumiya Janabekova (National Laboratory Astana) for SEM-EDS, and Prof. Izumi Taniguchi (Institute of Science Tokyo) for providing access to the TG-DTA.

References

1 Y. Li, Z. T. Wang, G. Liu, J. Wang and J. Wang, *Adv. Powder Technol.*, 2021, **32**, 4651–4657.
2 S. Ji, Y. Zheng, K. S. Hui, J. Li, K. Wang, C. Song, H. Xu, S. Wang, C. Zha, D. A. Dinh, Z. Tang, Z. Shao and K. N. Hui, *Energy Storage Mater.*, 2023, **57**, 400–410.
3 S. A. Haddadi, E. Alibakhshi, A. Labani Motlagh, S. A. A. Ramazani, M. Ghaderi, B. Ramezanzadeh, M. Mahdavian and M. Arjmand, *Prog. Org. Coat.*, 2022, **171**, 107055.
4 X. Chen, Z. Xu, Y. Liu, G. Li, S. Zhao, X. Zhang, Y. Wang, Y. Cao, C. Wang and Y. Xia, *Chem. Eng. J.*, 2025, **506**, 160014.
5 Y. Guo, Y. Liu, Y. Li, S. Hou, T. Liu and L. Zhao, *Appl. Surf. Sci.*, 2020, **508**, 145288.
6 L. Wang, G. Zhang, Q. Liu and H. Duan, *Mater. Chem. Front.*, 2018, **2**, 1414–1435.
7 Z. Tang, S. Zhou, Y. Huang, H. Wang, R. Zhang, Q. Wang, D. Sun, Y. Tang and H. Wang, *Electrochem. Energy Rev.*, 2023, **6**, 8.
8 S. Karimzadeh, B. Safaei, C. Yuan and T.-C. Jen, *Electrochem. Energy Rev.*, 2023, **6**, 24.
9 Y. Li, Y. Zhao, K. Chen, X. Liu, T. Yi and L.-F. Chen, *Acta Phys. – Chim. Sin.*, 2024, **40**, 2305007.
10 Z. Cao, Y. Zhu, K. Chen, Q. Wang, Y. Li, X. Xing, J. Ru, L. Meng, J. Shu, N. Shpigel and L. Chen, *Adv. Mater.*, 2024, **36**, 2401271.
11 W. Bi, C. Li, D. Yang, Y.-Z. Zhang, L. Hu, Q. Gong, J. Zhang, Y. Zhang, M. Li, J. Wei, Y. Zhou, D. Zhou, T. Wu, L.-F. Chen and A. Cabot, *Energy Environ. Sci.*, 2025, **18**, 1929–1940.
12 W. Li, L. Gan, K. Guo, L. Ke, Y. Wei, H. Li, G. Shen and T. Zhai, *Nanoscale*, 2016, **8**, 8666–8672.
13 X. He, X. Wang, M. Tang, H. Zhang and Y. Wang, *J. Alloys Compd.*, 2022, **897**, 163235.
14 S. Berikbaikyzy, Y. Sagynbay, G. Turarova, I. Taniguchi, Z. Bakenov and A. Belgibayeva, *Eurasian Chem.-Technol. J.*, 2023, **25**, 81.
15 A. Belgibayeva, M. Rakhatkyzy, A. Rakhmetova, G. Kalimuldina, A. Nurpeissova and Z. Bakenov, *Small*, 2023, **2304062**, 1–10.
16 G. Li, F. Hu, J. Chen, X. Fan, X. Xiao, L. Ma and L. Kong, *J. Mater. Chem. A*, 2024, **12**, 11535–11543.
17 A. Belgibayeva, S. Berikbaikyzy, Y. Sagynbay, G. Turarova, I. Taniguchi and Z. Bakenov, *J. Mater. Chem. A*, 2023, **11**, 11964–11986.
18 T. Zhang, D. Qiu and Y. Hou, *Nano Energy*, 2022, **94**, 106909.
19 R. Rošic, J. Pelipenko, P. Kocbek, S. Baumgartner, M. Bešter-Rogač and J. Kristl, *Eur. Polym. J.*, 2012, **48**, 1374–1384.

20 M. Akdere and T. Schneiders, *Modeling of the electrospinning process*, Elsevier Ltd, 2021.
21 G. W. Peterson and T. H. Epps, *Polymer*, 2022, **252**, 124816.
22 A. Belgibayeva and I. Taniguchi, *Electrochim. Acta*, 2019, **328**, 135101.
23 M. G. McKee, G. L. Wilkes, R. H. Colby and T. E. Long, *Macromolecules*, 2004, **37**, 1760–1767.
24 S. Kandasamy, V. Narayanan and S. Sumathi, *Int. J. Biol. Macromol.*, 2020, **145**, 1018–1030.
25 G. Turarova, I. Taniguchi, Z. Bakenov and A. Belgibayeva, *J. Power Sources*, 2024, **613**, 234933.
26 M. Pudukudy, Z. Yaakob, R. Rajendran and T. Kandaramath, *React. Kinet., Mech. Catal.*, 2014, **112**, 527–542.
27 B. Boonchom, R. Baitahe, S. Kongtaweelert and N. Vittayakorn, *Ind. Eng. Chem. Res.*, 2010, **49**, 3571–3576.
28 S. Mintova and J. Čejka, *Stud. Surf. Sci. Catal.*, 2007, **168**, 301–326.